nature portfolio

https://doi.org/10.1038/s41566-022-00978-0

Supplementary information

Large-scale planar and spherical light-emitting diodes based on arrays of perovskite quantum wires

In the format provided by the authors and unedited

Supplementary Information for:

Large-scale planar and spherical light-emitting diodes based on arrays of perovskite quantum wires

Daquan Zhang[1], Qianpeng Zhang[1], Beitao Ren[1], Yudong Zhu[1,3], Mohamed Abdellah[4,5], Yu Fu[1], Bryan Cao[1], Chen Wang[1], Leilei Gu[1], Yucheng Ding[1], Kwong-Hoi Tsui[1], Sufeng Fan[6], Swapnadeep Poddar[1], Lei Shu[1], Yuting Zhang[1], Dai-Bin Kuang[7], Jin-Feng Liao[7], Yang Lu[6], Kaibo Zheng[4,8], Zhubing He[3], Zhiyong Fan[1,2]✉

[1]Department of Electronic and Computer Engineering, The Hong Kong University of Science and Technology, Clear Water Bay, Kowloon, Hong Kong SAR, China

[2]Guangdong-Hong Kong-Macao Joint Laboratory for Intelligent Micro-Nano Optoelectronic Technology, HKUST, Clear Water Bay, Kowloon, Hong Kong SAR, China

[3]Department of Materials Science and Engineering, Shenzhen Key Laboratory of Full Spectral Solar Electricity Generation (FSSEG), Southern University of Science and Technology, Shenzhen, Guangdong, 518055, China.

[4]Department of Chemical Physics and NanoLund, Lund University, Box 124, 22100 Lund, Sweden

[5]Department of Chemistry, Qena Faculty of Science, South Valley University, 83523 Qena, Egypt

[6]Department of Mechanical Engineering, City University of Hong Kong, Hong Kong SAR, China

[7]MOE Key Laboratory of Bioinorganic and Synthetic Chemistry, Lehn Institute of Functional Materials, School of Chemistry, Sun Yat-sen University, Guangzhou 510275, P. R. China

[8]Department of Chemistry, Technical University of Denmark, DK-2800 Kongens Lyngby, Denmark

✉Corresponding author: eezfan@ust.hk

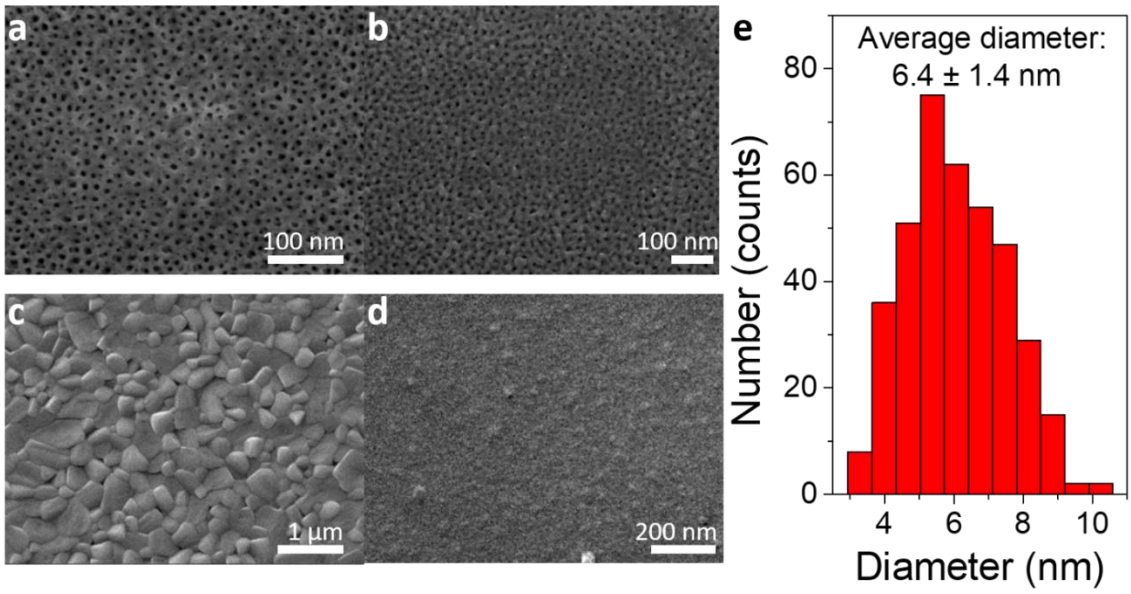

Supplementary Figure 1. Morphology characterization. a-d, top view SEM images of the chip after different growth steps: no growth (**a**), little growth (**b**), over growth (**c**), and surface clean (**d**). **e**, 5 V PAM pore size histogram distribution extracted from SEM image in **a**.

Supplementary Fig. 1a-d show the top-view scanning electron microscopy (SEM) images of the chip after different growth steps. Specifically, Supplementary Fig. 1a shows the 5 V PAM with Pb deposited before QWs growth. After a short time CSVR growth, some pores are filled with materials (Supplementary Fig. 1b). As the growth continues, the materials will grow outside of the PAM channels and form a layer of bulk film with ~ 500 nm grain size at the top surface (Supplementary Fig. 1c). As discussed in the main text, the surface bulk $MAPbBr_3$ is showing very poor PLQY, which will hurt the LEDs device performance. So, followed by a regrowth process, an ion milling process is carried out to clean the surface (Supplementary Fig. 1d).

The PAM pore size histogram distribution was extracted from Supplementary Fig. 1a and shown in Supplementary Fig. 1e, to precisely describe the pore diameter. Specifically, the nanopores are semi-ordered on the substrate with average diameters of 6.4 ± 1.4 nm, which subsequently determine the diameters of both deposited Pb NW precursor and grown $MAPbBr_3$ QWs. Meanwhile, the 5 V PAM has an ultra-high pore density, up to ~10^{12} cm^{-2}. This unique feature of PAM will consequently contribute to ultra-high density perovskite QW arrays with every single QW well isolated, which will be extremely promising for the micro-LEDs application in the future.

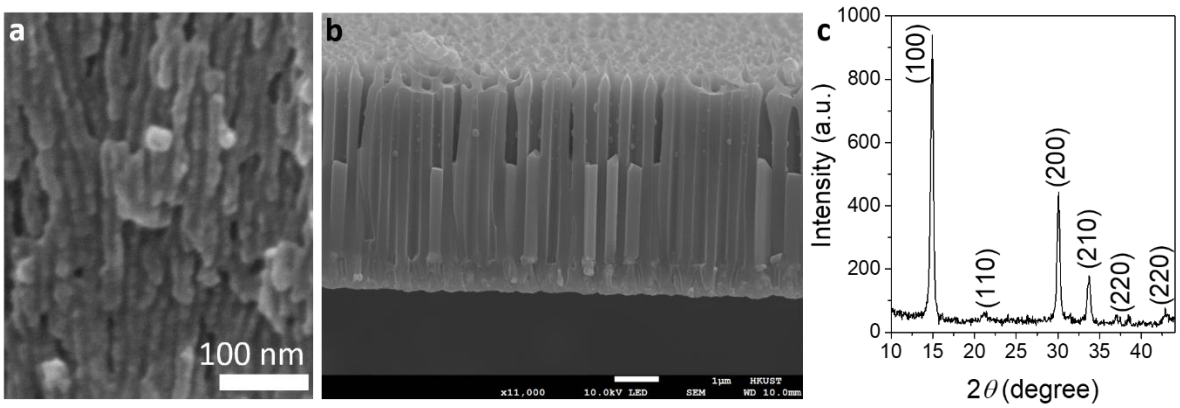

Supplementary Figure 2. SEM images of $MAPbBr_3$ QW (a) and NW (b) arrays grown using the same CSVR in 5 V and 200 V PAMs, respectively, and XRD pattern of $MAPbBr_3$ QW arrays (c).

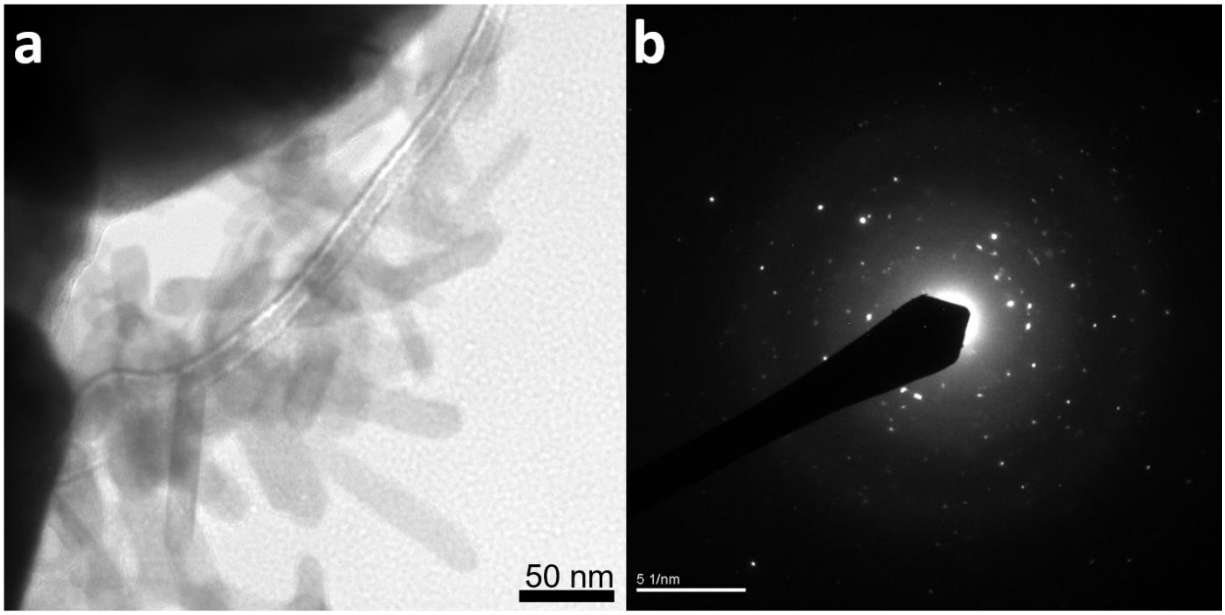

Supplementary Figure 3. TEM characterization of $MAPbBr_3$ QWs. a, A TEM image of several $MAPbBr_3$ QWs stacked together extracted from 5 V PAM. **b,** SAED pattern of the QWs shown in **a**.

High resolution transmission electron microscopy (HRTEM) image of $MAPbBr_3$ QWs is shown in Supplementary Fig.3a. For TEM specimen preparation, the $MAPbBr_3$ QWs are extracted from 5 V PAM by using a grind and sonication process without damaging their crystallinity. Selected area electron diffraction (SAED) pattern of those QWs was obtained and shown in Supplementary Fig. 3b, where there is no uniform crystal orientation observed. Hence, although every single QW is crystalline, different QWs have different growth orientations since the electrochemically deposited Pb metal precursor and the metal-assisted CVD growth happen in every isolated PAM channels. The growth is random for the QW or NW arrays[1,2]. The result is in consistent with the QWs XRD pattern shown in Supplementary Figure 2c.

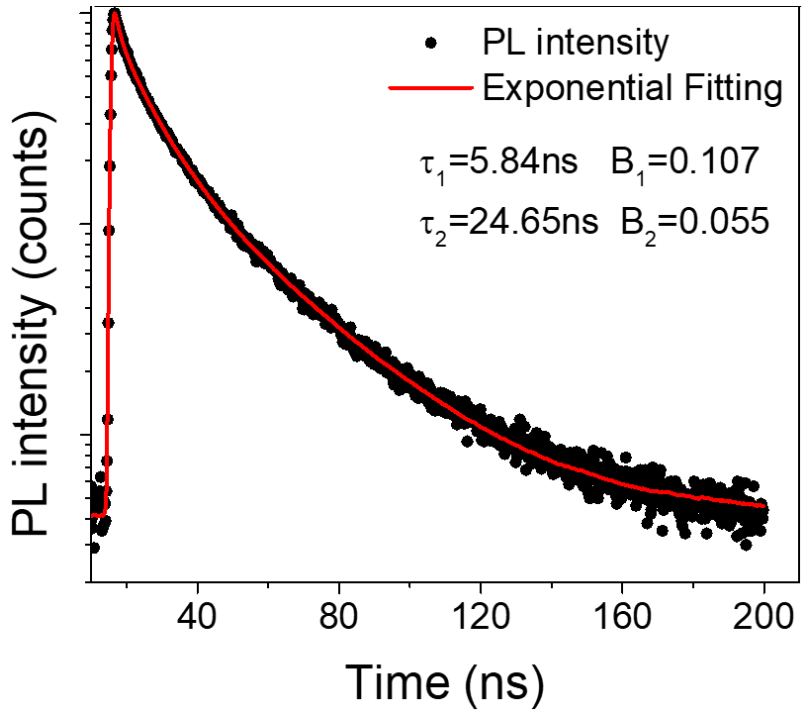

Supplementary Figure 4. Carrier lifetime measurement.

Time-resolved photoluminance (TRPL) was measured to characterize the carrier lifetime of $MAPbBr_3$ QWs with the utilization of a 365 nm pulsed LEDs and time-correlated single photon counting (TCSPC). A double-exponential function was used to fit the PL decay profile:

$$I(t) = A + B_1 e^{(-t/\tau_1)} + B_2 e^{(-t/\tau_2)}, \quad (1)$$

The average lifetime is given by:

$$\tau_{ave} = \frac{\tau_1 * B_1 + \tau_2 * B_2}{B_1 + B_2}. \quad (2)$$

An average carrier lifetime of 12.2 ns can be obtained from Supplementary Fig. 4. Such short carrier lifetime dedicates the high radiative recombination rate in $MAPbBr_3$ QWs[2].

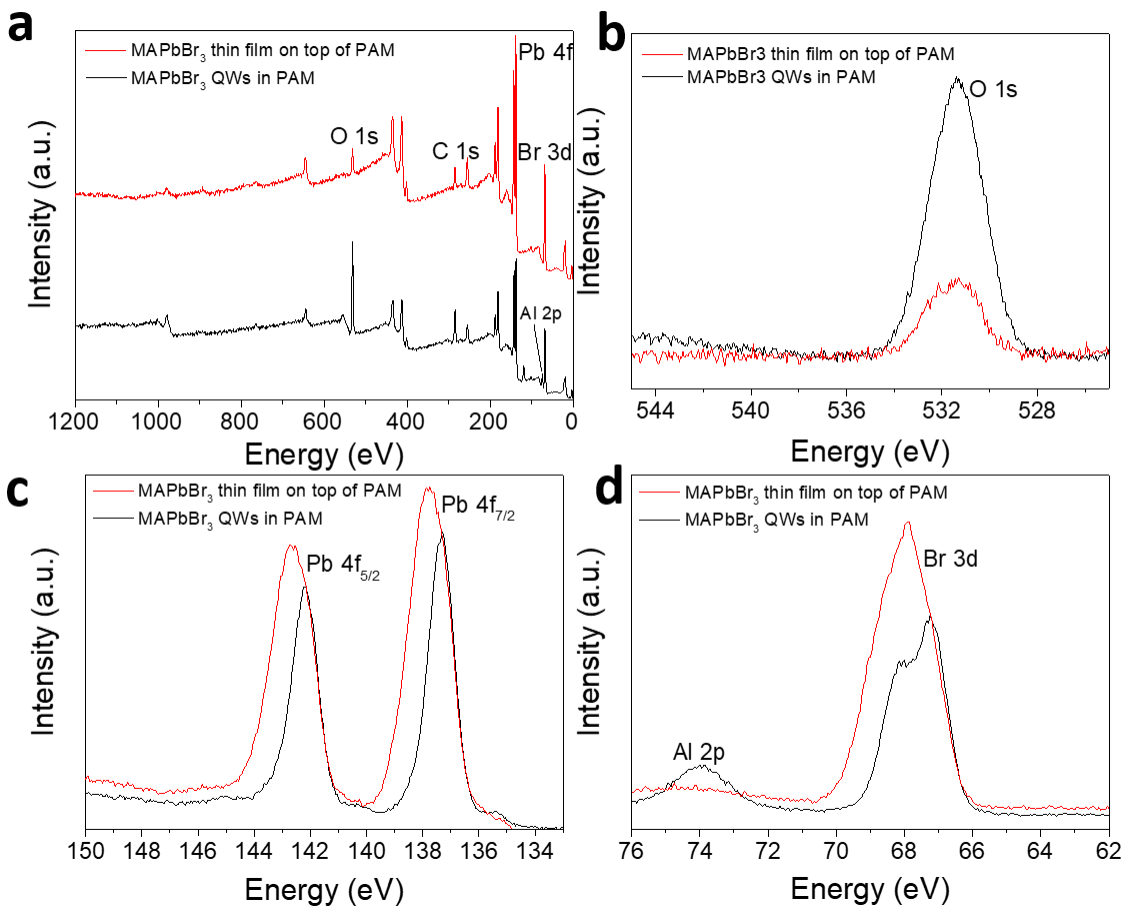

Supplementary Figure 5. XPS measurement. a, Survey-scan XPS spectra of $MAPbBr_3$ thin film on top of PAM and QWs in PAM. **b-d,** High resolution XPS spectra of O 1s (**b**), Pb ($4f_{5/2}$, $4f_{7/2}$) (**c**), Al 2p and Br 3d (**d**) of $MAPbBr_3$ thin film on top of PAM and QWs in PAM.

To prove the surface passivation effect, XPS analysis was carried out to study the surface chemical condition of the $MAPbBr_3$ QWs in PAM. As a control sample, $MAPbBr_3$ thin film on top of PAM (the sample shown in Figure 1d1 and 1d2) was also characterized. All the XPS spectra were calibrated using the C 1s peak at 285.0 eV. From the survey scan spectra in Supplementary Figure 5a, the presence of $MAPbBr_3$ and Al_2O_3 can be clearly observed. Specifically, the peaks at 531.3 eV and 74.0 eV can be assigned to the binding energies of O 1s and Al 2p, respectively, revealing the presence of Al_2O_3. The Pb 4f spectrum for $MAPbBr_3$ QWs in PAM has been recorded with two contributions of Pb $4f_{5/2}$ and $4f_{7/2}$ at 142.2 eV and 137.3 eV. It is interesting that there is a slight shift to lower binding energy of Pb 4f peaks, compared with that of $MAPbBr_3$ thin film on

top of PAM sample (142.6 eV and 137.8 eV). It can be attributed to the Pb-rich surface defects which are passivated by the oxygen after growing the $MAPbBr_3$ in the PAM substrate, which in turn can significantly suppress non-radiative recombination on the QWs surface.[3] Meanwhile, Our CSVR growth starts from the electrochemically deposited Pb metal in Al_2O_3 substrate under high temperature, especially for $CsPbBr_3$ QWs grown under 400 ^oC condition. It can easily form the Pb-O bonding on the PAM sidewall during the growth process, which distorts and tilts the $PbBr_6$ octahedral and hence results in a lattice contraction of QWs in PAM[4]. With these evidences, it can be claimed that the surface of QWs is chemically and physically passivated by the PAM, contributing to the excellent thermal and humidity-stability, as well as high PLQY, as discussed in the main text.

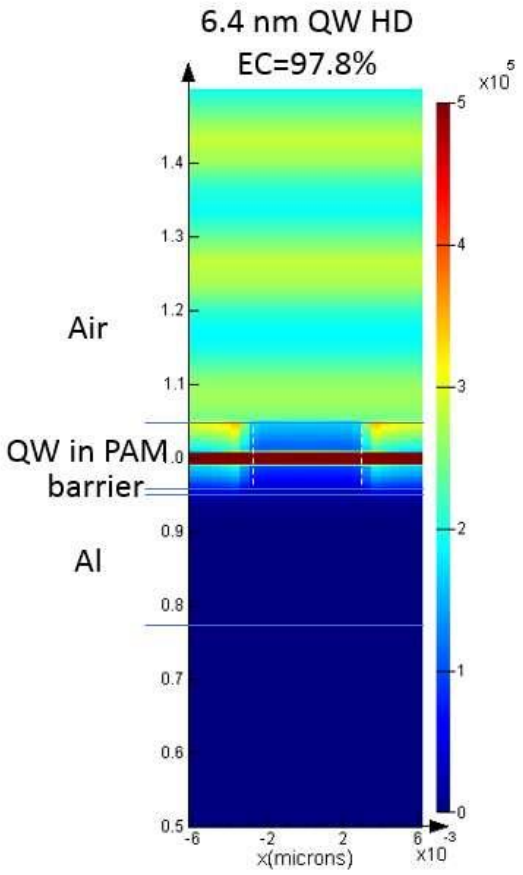

Supplementary Figure 6. Simulated light out-coupling efficiency of $MAPbBr_3$ QWs.

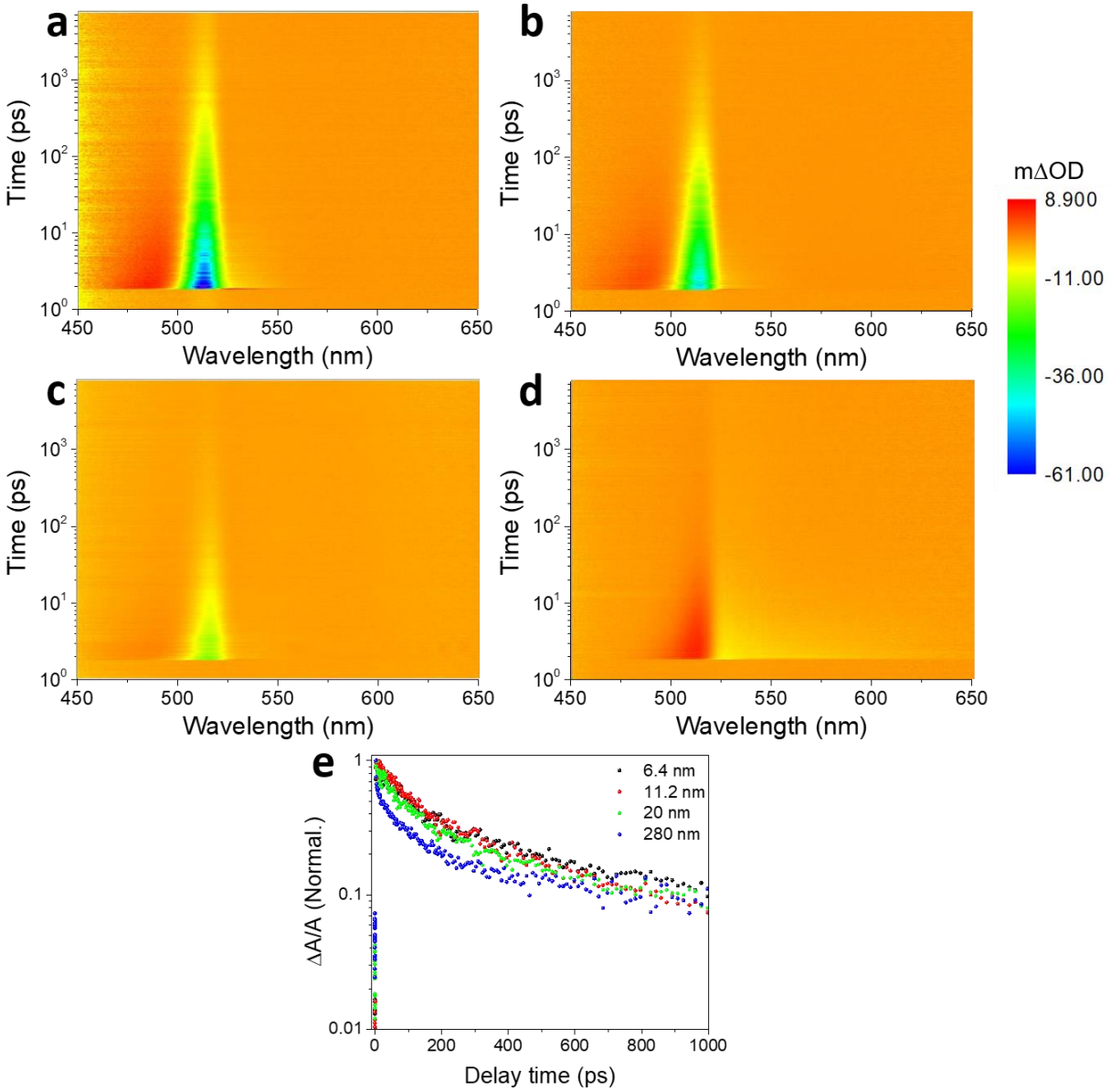

Supplementary Figure 7. TA measurement. a-d, TA mappings of different QWs after pulse excitation as the function of wavelength and delay time: **a,** 6.4 nm, **b,** 11.2 nm, **c,** 20 nm, and **d,** 280 nm diameter NWs. **e**, kinetic TA signals of different diameters NW arrays.

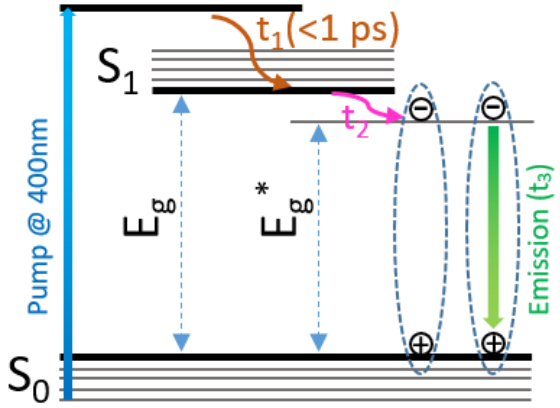

Supplementary Figure 8. Schematic illustration of the photo-physical processes involved in QWs

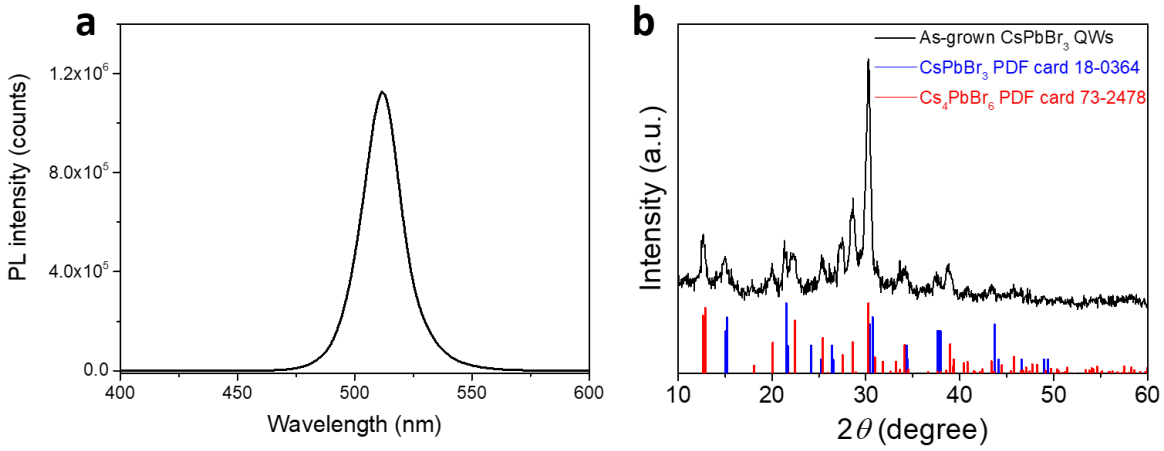

Supplementary Figure 9. $CsPbBr_3$ QWs characterization. The PL spectrum (a) and XRD pattern (b) of $CsPbBr_3$ QWs.

The PL spectrum of $CsPbBr_3$ QWs grown in the PAM is shown in Supplementary Fig. 9a. The PL peak position is located at 511.5 nm, corresponding to a band gap of 2.42 eV. Comparing with the band gap of a $CsPbBr_3$ thin film (2.3 eV), the obvious band increase can be attributed to the quantum confinement effect, as discussed in the main text. The narrow FWHM of 19 nm indicates very high-purity green emission, which is even better than most of the $CsPbBr_3$ crystals[5]. The XRD pattern of the grown QWs is demonstrated in Supplementary Fig. 9b. It is interesting that the QWs XRD pattern is the combination of two standard patterns (PDF card 18-0364 and 73-2478), revealing the mixture phase of $CsPbBr_3$ and Cs_4PbBr_6 in the QWs. It is well known that Cs_4PbBr_6 has a 0D perovskite structure and can exhibit more than one order of magnitude higher PL intensity than $CsPbBr_3$[6], which counts for the high PLQY of our grown $CsPbBr_3$ QWs, as well as the quantum confinement effect.

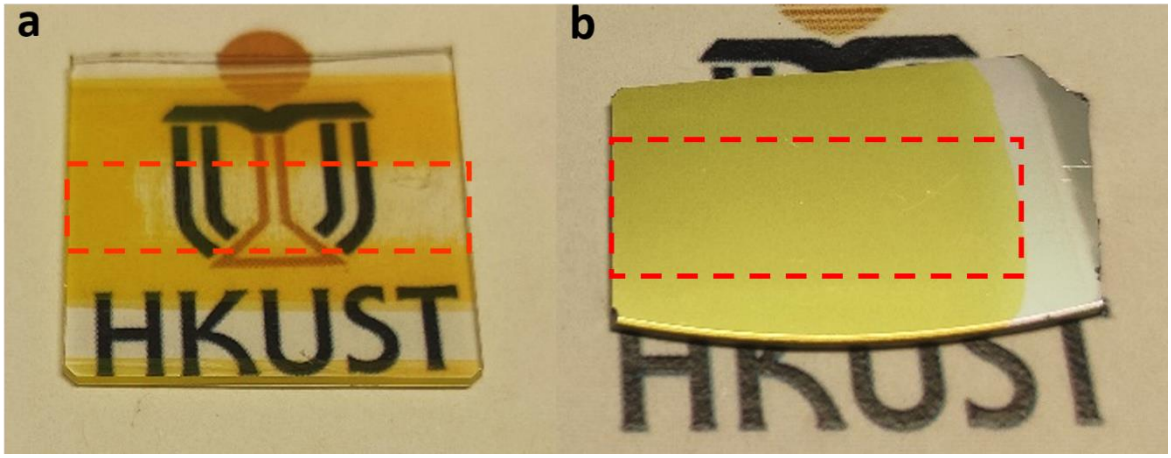

Supplementary Figure 10. Mechanical stability test. Digital photos of the $MAPbBr_3$ thin film (**a**) and QWs in PAMs (**b**) after peel test. The marked area is tape-contacted area. It is clear that the thin film sample is delaminated after 300 peel test cycles. On the contrary, there is almost no change with the QWs sample after 1,000 cycles.

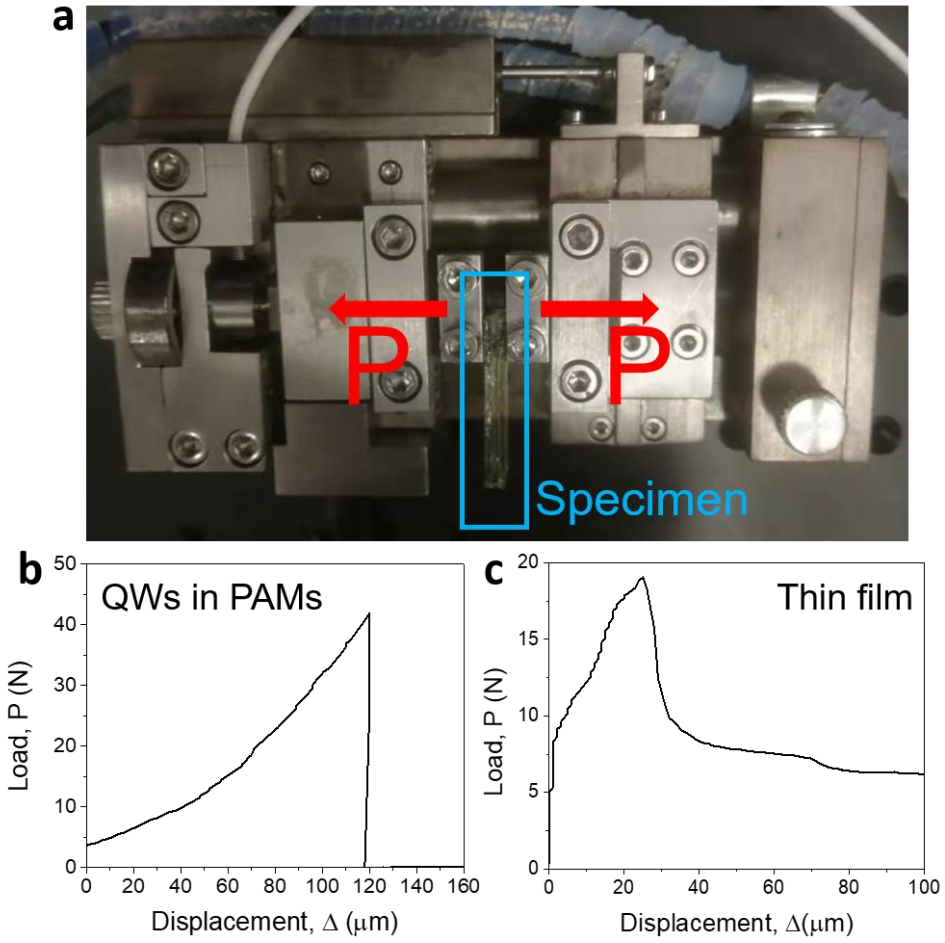

Supplementary Figure 11. Thin film cohesion testing. a. A digital photo of the DCB for the load-displacement measurement. The specimen was made from two glass slides and the sandwiched perovskite thin film with the use of NOA81 UV epoxy. The whole specimen was bonded to the beam using 502 fast curing epoxy. **b, c,** Load-displacement curves for $MAPbBr_3$ QWs in PAMs (**b**) and thin film counterpart (**c**).

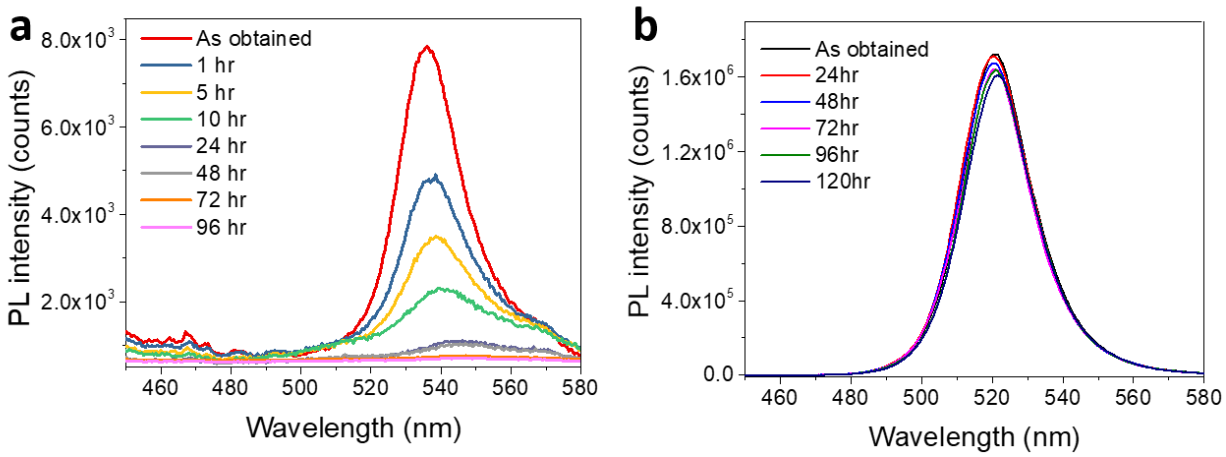

Supplementary Figure 12. Humidity stability test. PL spectra evolution over time of $MAPbBr_3$ thin film (**a**) and QWs (**b**) in ambient air condition.

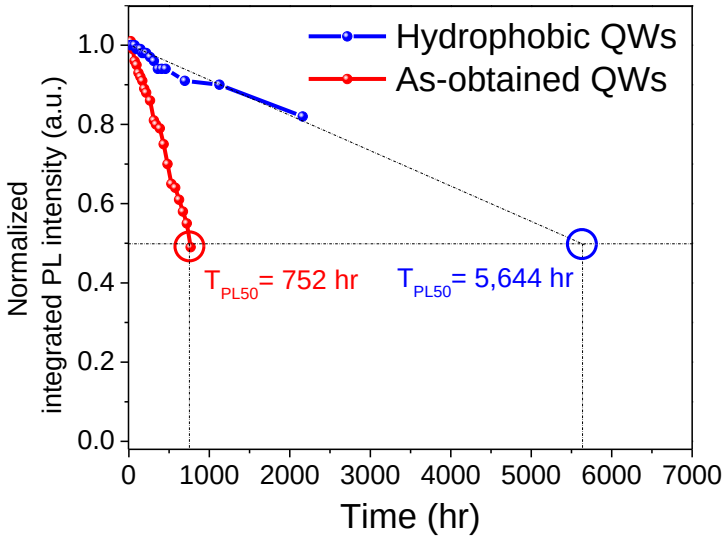

Supplementary Figure 13. PL lifetime of as-obtained QWs and hydrophobic QWs.

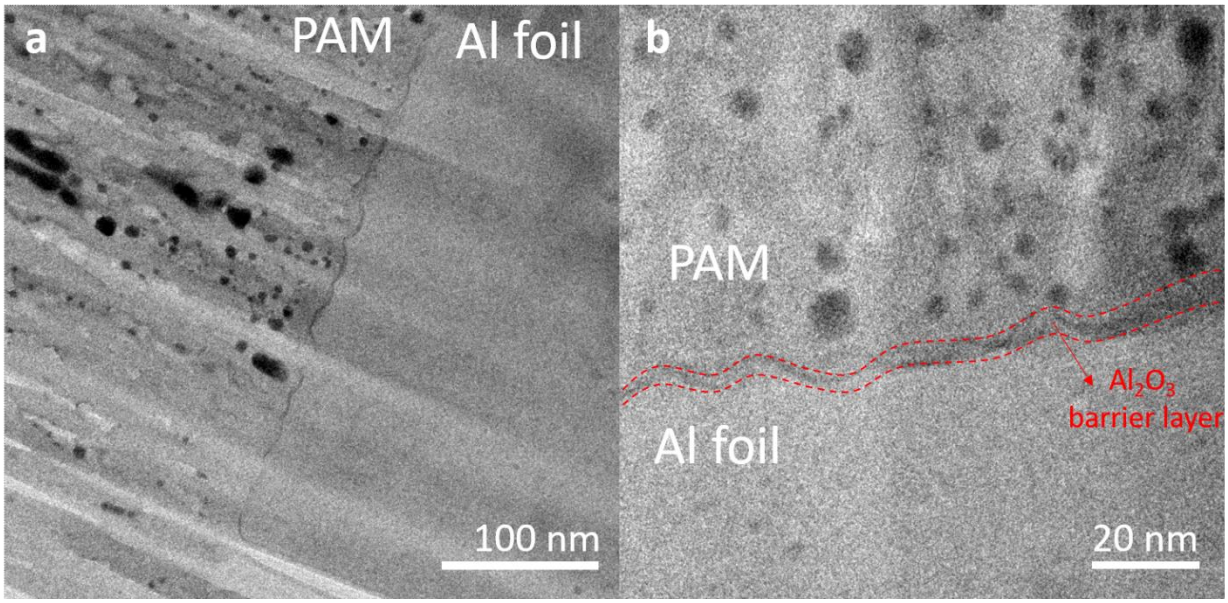

Supplementary Figure 14. Cross-sectional TEM images of a 5 V PAM showing the existence of an ultrathin Al_2O_3 barrier layer.

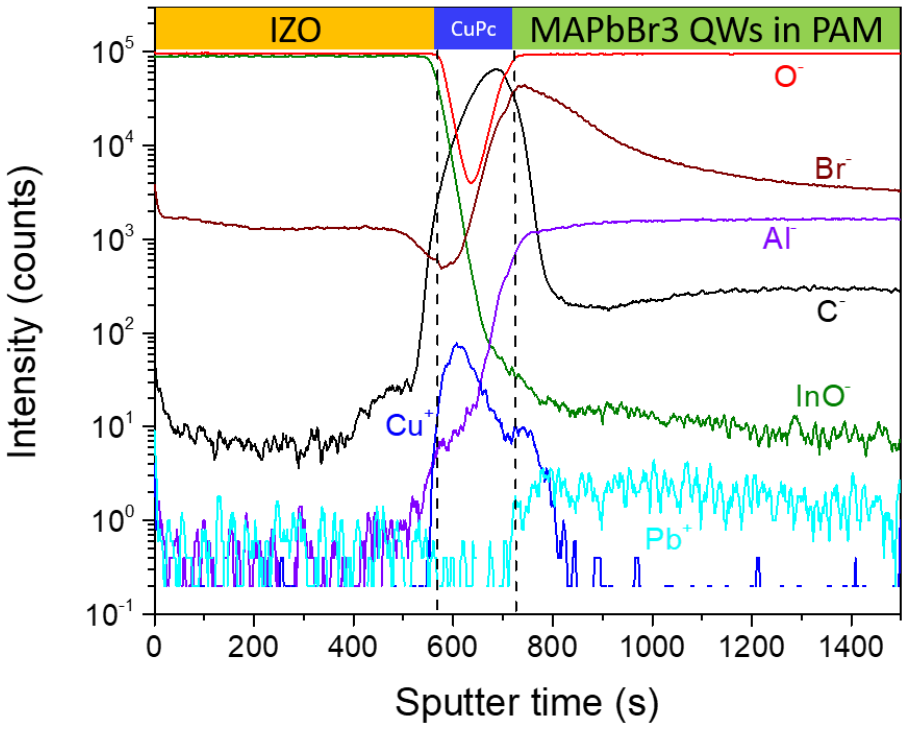

Supplementary Figure 15. ToF-SIMS characterization of the $MAPbBr_3$ QWs based LED device.

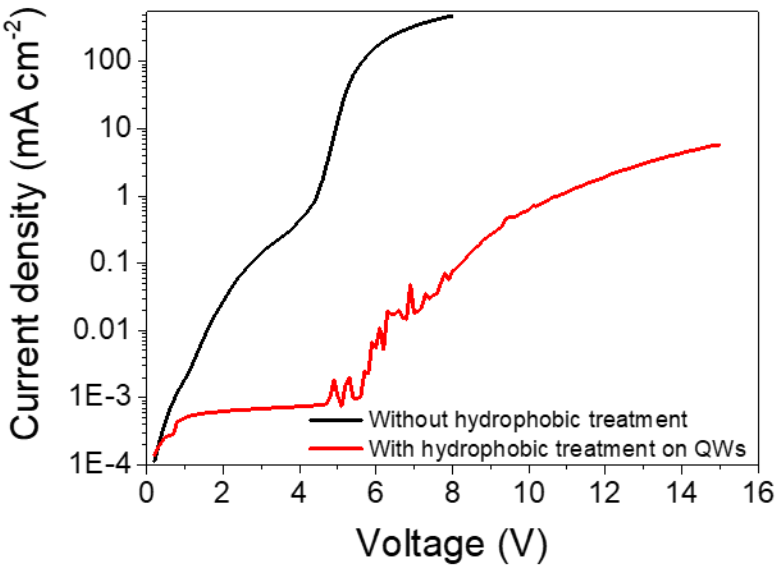

Supplementary Figure 16. *J-V* curves of the LED devices with and without hydrophobic treatment on the QWs.

Experimentally, after the hydrophobic treatment on the QWs, no significant performance improvement is observed as far as EQE and luminance concerned. More specifically, if the hydrophobic treatment was carried out on the QWs/PAM surface before device fabrication, the extra hydrophobic layer will block the carrier injection severely thus the current level is several orders lower and indiscernible EL light can be observed after the treatment, as shown in the Supplementary Figure 16. And if it is conducted on a completed device, it is very similar to the case of the device without treatment in glovebox environment (as shown in main text Fig. 5c), where it is the electrical stability, rather than humidity stability, dominates device life time. Even though the hydrophobic treatment is not helping too much on the LEDs performance at this moment, it is still useful when our QWs arrays simply work as luminescent backplanes (color conversion) for large area displays, where the PL humidity stability is more critical.

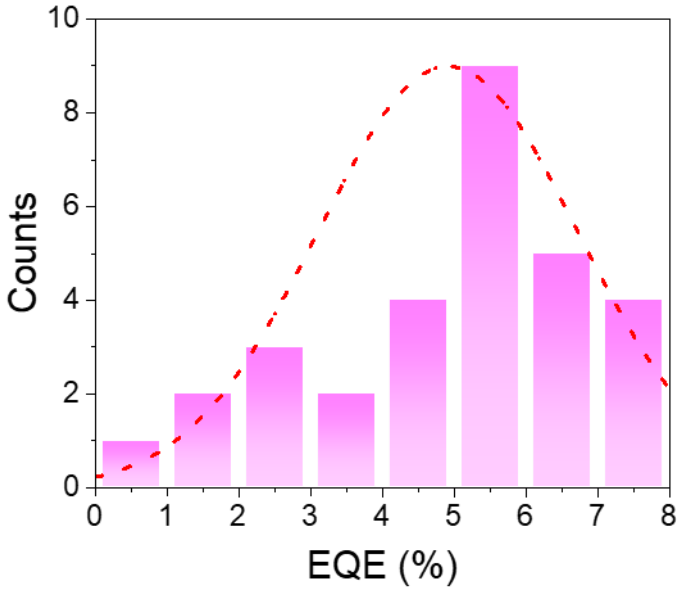

Supplementary Fig. 17. Histogram of the EQE distribution of $MAPbBr_3$ QWs LEDs.

There are totally 30 devices counted for the histogram of the $MAPbBr_3$ QWs EQE distribution. The device has an average EQE of 4.92 % with 0.51 % standard deviation.

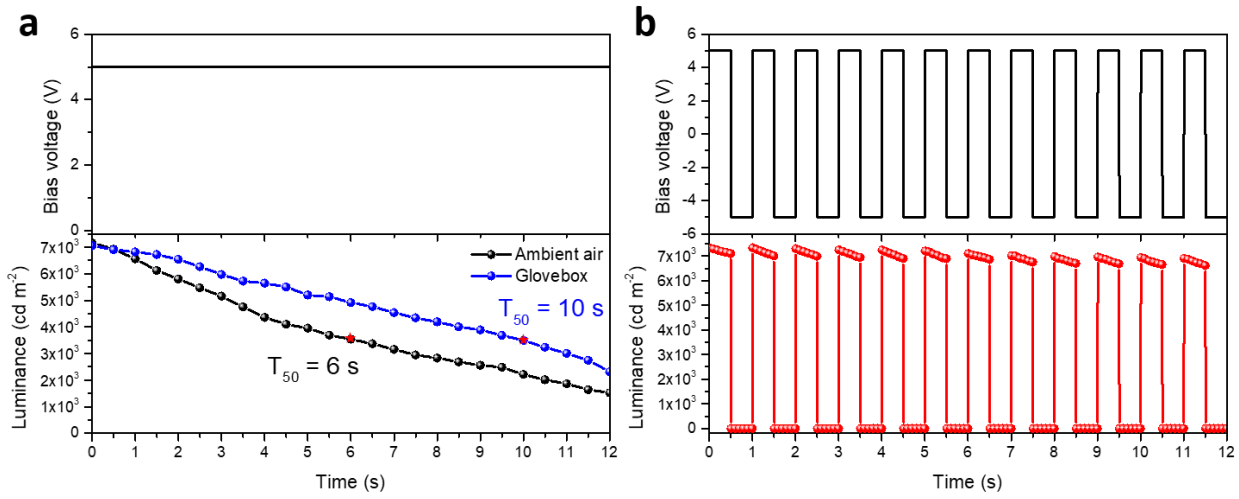

Supplementary Figure 18. Luminance decays of $MAPbBr_3$ QWs based LEDs under DC (a) and AC (b) bias.

Supplementary Fig. 18a shows the time domain luminance decay curve for L_0 around 7,000 cd m^{-2}. Intriguingly, there is no obvious improvement for this case when measured in glovebox. Supplementary Fig. 18b shows the luminance decay with 1 Hz AC bias applied. The luminance was still initially around 7,000 cd m^{-2}, and started to decay normally during the positive bias period. But after the negative bias period (EL off period), the luminance was recovered to be around L_0 again. This could be attributed to the ion recovery and less heat generation during the negative bias period.

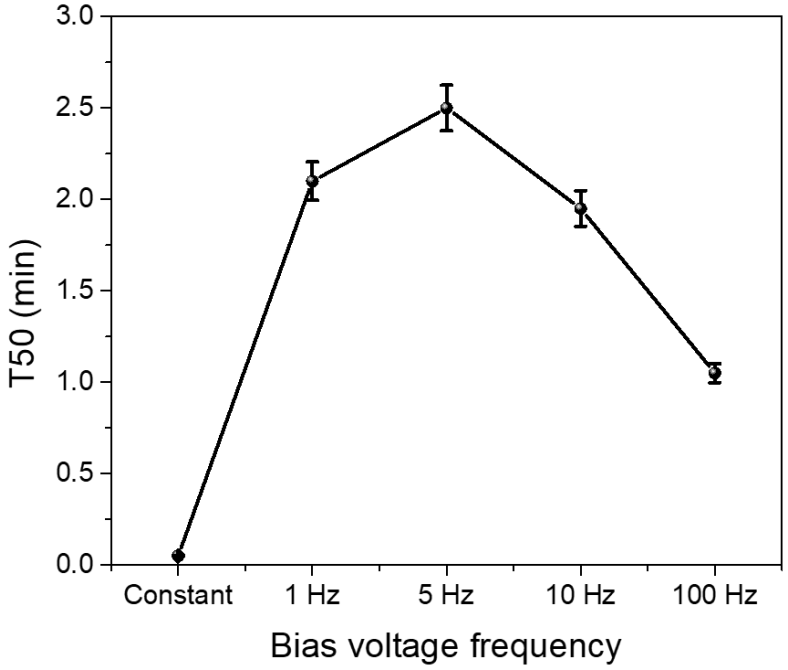

Supplementary Figure 19. Bias frequency dependent T_{50}. Each error bar indicates a standard deviation of ± 5 %.

We further tested the impact of frequency on the device operation. One thing should be mentioned that for 100 Hz bias, a higher injection level is needed to reach the same L_0 because of the RC delay in the circuit. Specifically, when the voltage switching speed is much higher than the RC delay, the current injection cannot ramp up to the max value during the positive period. Therefore, a higher voltage was needed to speed up the current ramping to reach the same L_0, which however will reversely result in the T_{50} and EQE drop. Supplementary Fig. 19 shows the T_{50} of the device under different frequencies bias with the same L_0 (~ 10, 000 cd m^{-2}). It can be seen that, compared with constant bias, the AC operation mode is beneficial to the lifetime improvement. But when the frequency is higher than 10 Hz, the T_{50} starts to decrease because too high bias amplitude is needed[7,8].

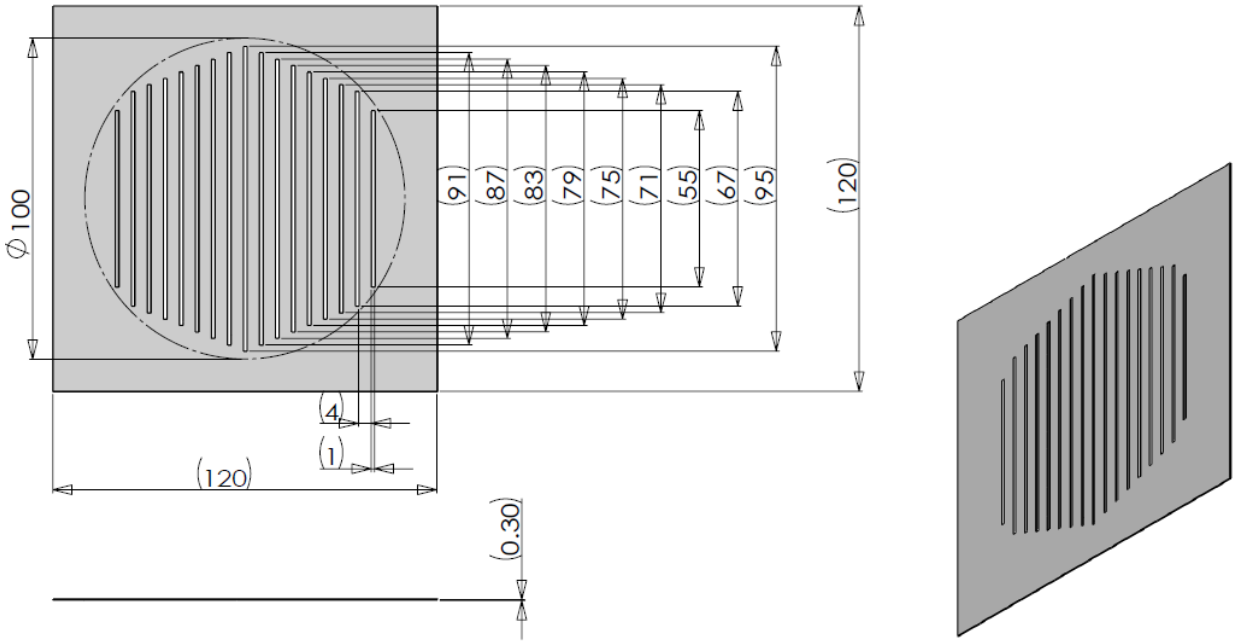

Supplementary Figure 20. Shadow mask design for gridline electrode deposition. The unit is mm.

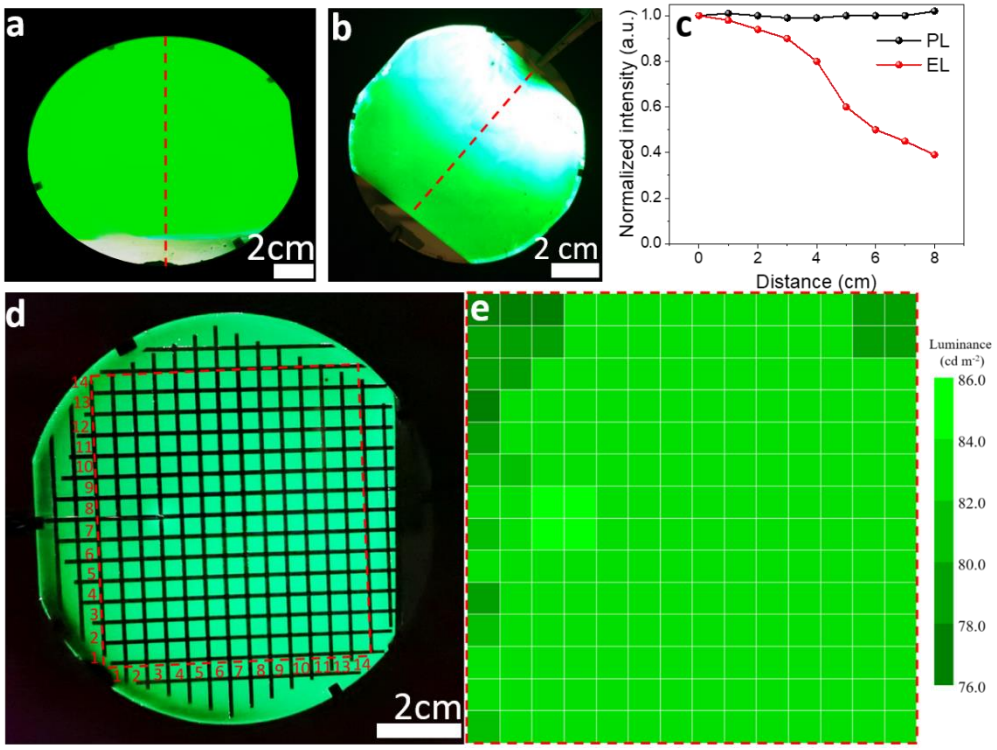

Supplementary Figure 21. PL and EL uniformity analysis. a, b, The PL (**a**) and EL (**b**) images shown in main text. **c**, Normalized PL and EL intensity sampling along the dash lines marked in **a** and **b**. The interval is 1 cm. Intensity is normalized by the first spot signal intensity. **d,** EL image shown in main text Figure 5f. **e,** EL intensity mapping of the selected area in **d**.

From the Supplementary Fig. 21, we can see that the PL intensity is quite uniform across the whole wafer with less than 2 % intensity variation, which reveals the excellent QW uniformity in 4-inch wafer scale. However, the EL intensity is gradually decreasing when the spot moves away from the positive electrode clip at the right side (Supplementary Fig. 21b and c). The main reason is the poor conductivity of our sputtered IZO and evaporated thin Au electrode in large scale size, which causes the bias voltage loss due to the series resistance. Meanwhile, the poor conductivity of our top electrodes also generates a lot of joule heat, which will kill the device within one minute. However, after applying an extra current distribution layer (thick Au gridlines), the EL uniformity is significantly improved (Supplementary Figure 21d). Because of the large size of the wafer device, the whole area luminance distribution cannot be measured pixel by pixel in time before the

device luminance changes. Therefore, only the luminance of pixel (11) (L_{p11}) in Supplementary Figure 21d was measured by an optical fiber. Then, the luminance values of other pixels were calibrated with respect to L_{p11} according to EL image brightness at each pixel. The EL intensity mapping of the selected area is shown in Supplementary Figure 21e. It can be seen that the EL uniformity is significantly improved as compared to the wafer scale device without the current spreading gridlines. We believe that this 4-inch wafer device performance, including the EL uniformity and stability, can be further improved by optimizing the sputtering conditions or utilizing Ag NWs as top electrode.

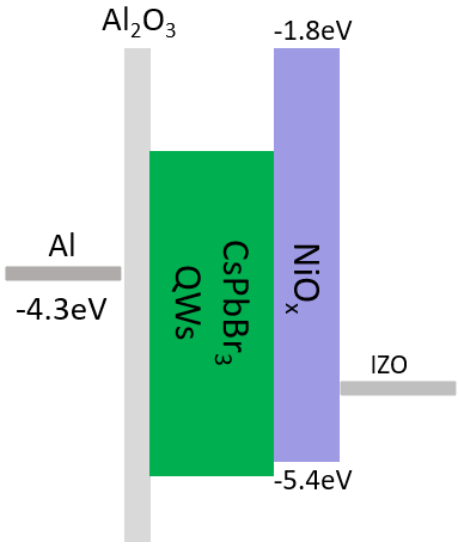

Supplementary Figure 22. Schematic band alignment for a $CsPbBr_3$ QWs based device showing Al/Al_2O_3/$CsPbBr_3$ QWs/NiO_x/IZO structure. The planar and spherical devices have the same structure.

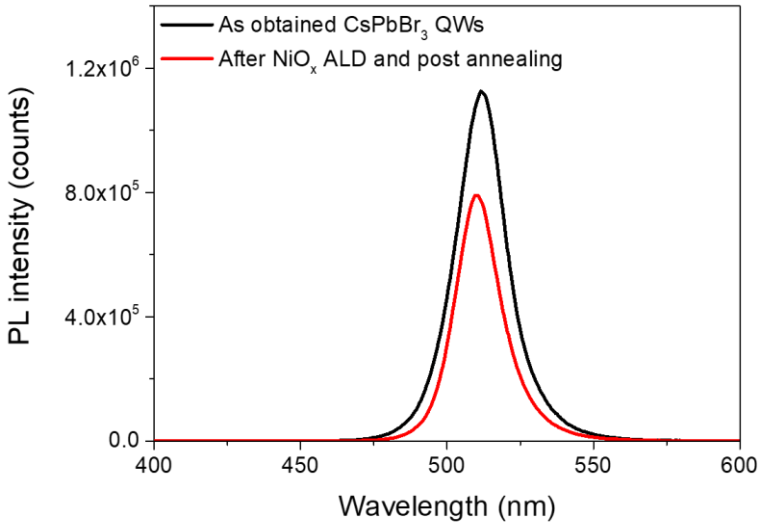

Supplementary Figure 23. PL spectra of $CsPbBr_3$ QWs before and after NiO_x ALD and post annealing (300 ºC in air for 1 hr).

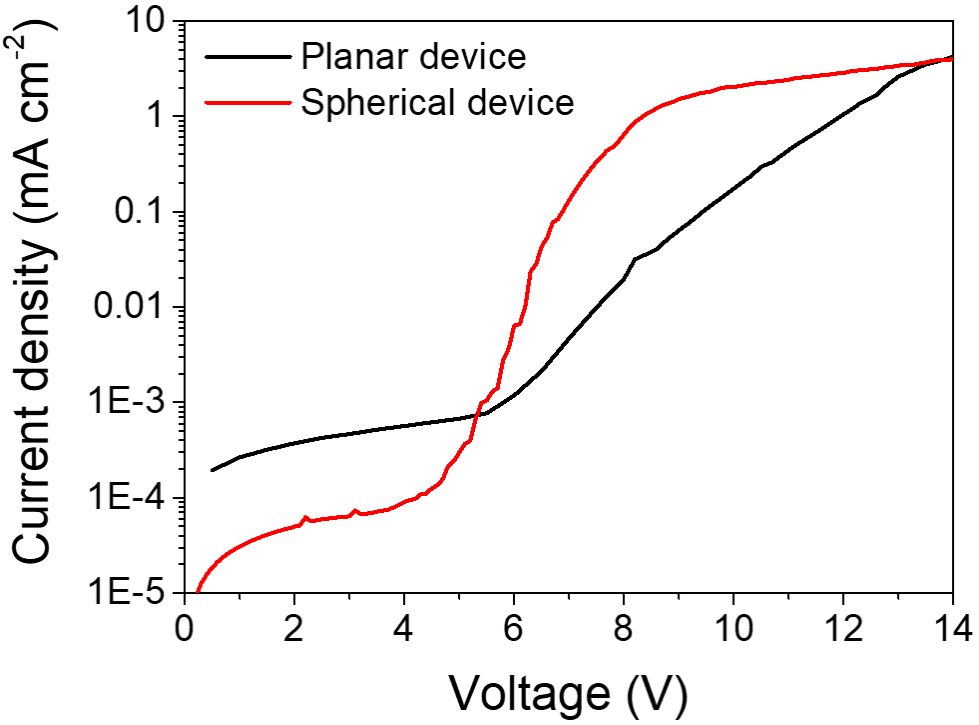

Supplementary Figure 24. ***J-V*** **curve of the planar (black) and 3-D spherical (red) device. IZO and Al are positive and negative electrodes, respectively.**

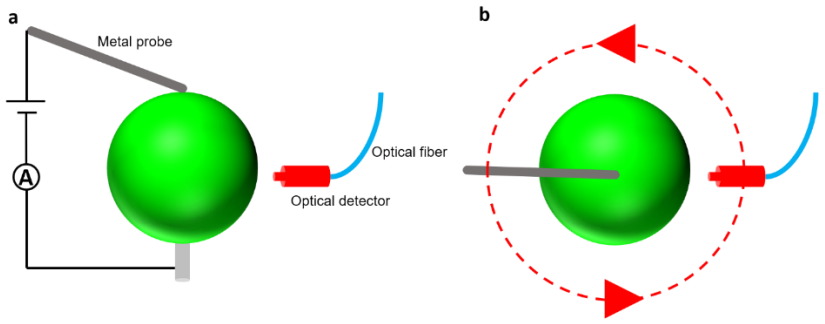

Supplementary Figure 25. 3-D spherical device measurement schematics. a, side view. **b**, top view.

The spherical device measurement is described schematically in Supplementary Figure 25. The negative bias is applied to the Al rod and the positive bias is applied to a metal probe contacting the IZO electrode. The optical spectrometer is ~ 2 cm far away from the device, and rotates along the equator line of the sphere to get the angular luminance distribution. For every angular spot, the measurement area is only 0.2826 mm^2, same with the optical fiber detection area (0.6 mm in diameter). The measurement integration time for every spot is 100 ms, and every movement takes 0.5 s.

Supplementary Table 1. TA charge Lifetime values (t_2 and t_3) for different QW arrays obtained from a triple-exponential tail fitting.

	A_1 (%)	t_1 (ps)	A_2 (%)	t_2 (ps)	A_3 (%)	t_3 (ps)	$T_{average}$ (ps)
6.4 nm	5.4	Inf	60.5	95.4	34.1	813	334.95
11.2 nm	3.0	Inf	64.2	107	32.8	660	285.17
20 nm	7.6	Inf	60.2	75.2	32.2	543	220.12
280 nm	9.2	Inf	75.1	78.8	15.7	887	198.44

The charge lifetime values of different QWs are extracted from a triple-exponential fittings of the kinetic TA signals at the GBS wavelength shown in the Supplementary Figure 7. The fitting function used for the TA decay profile is as followings[9]:

$$\Delta A(t) = A_1 e^{(-t/t_1)} + A_2 e^{(-t/t_2)} + A_3 e^{(-t/t_3)} \quad (3)$$

The fast decay time (t_1), mediate decay time (t_2) and slow decay time (t_3) are ascribed to the cooling of above-bandgap photogenerated charges, the exciton formation resulted from the quantum confinement effect, and radiative exciton recombination processes, respectively, as presented in the Supplementary Figure 8. Since the charge cooling process is too shot (<1 ps) compared with other two time constant, infinite small (Inf) value is used for the fitting. The average lifetime is given by:

$$\tau_{ave} = A_2 t_2 + A_3 t_3. \quad (4)$$

The average lifetime is increased from 198.44 ps to 334.95 ps when decreasing the NWs diameter from 280 nm to 6.4 nm, which means stronger excitonic radiative recombination for QWs because of the quantum confinement effect[9]. The result is consistent with the PLQY trend discussed in the main text.

Supplementary Table 2. Fluorescent images of $MAPbBr_3$ thin film and QWs under different testing conditions. The size for all samples is the same 1 cm × 1 cm.

	Ambient air (23 ℃, 45 - 55 % RH)		
	as obtained	after 5 days	after 30 days
$MAPbBr_3$ thin film		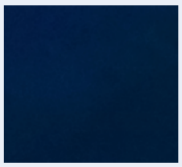	NA
As-obtained QWs in PAM	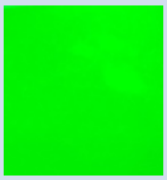	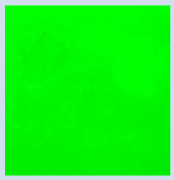	
QWs in hydrophobic PAM			

Supplementary Video 01: Water stability demonstration of $MAPbBr_3$ QWs in PAM with hydrophobic surface.

Supplementary Video 02: Real-time measurement of a perovskite LED device with voltage scanning from 0-8v.

Supplementary Video 03: 2-axis rotation for electrode deposition on the 3-D spherical device.

References

1. Gu, L. *et al.* 3D Arrays of 1024-Pixel Image Sensors based on Lead Halide Perovskite Nanowires. *Adv. Mater.* **28**, 9713-9721, (2016).
2. Zhang, D. *et al.* Increasing Photoluminescence Quantum Yield by Nanophotonic Design of Quantum-Confined Halide Perovskite Nanowire Arrays. *Nano Lett.* **19**, 2850-2857, (2019).
3. Wang, X. D. *et al.* Surface passivated halide perovskite single-crystal for efficient photoelectrochemical synthesis of dimethoxydihydrofuran. *Nat Commun* **12**, 1202, (2021).
4. Liu, M. *et al.* Aluminum-Doped Cesium Lead Bromide Perovskite Nanocrystals with Stable Blue Photoluminescence Used for Display Backlight. *Advanced Science* **4**, 1700335, (2017).
5. Diroll, B. T., Nedelcu, G., Kovalenko, M. V. & Schaller, R. D. High‐temperature photoluminescence of CsPbX3 (X= Cl, Br, I) nanocrystals. *Adv. Funct. Mater.* **27**, 1606750, (2017).
6. Cha, J. H. *et al.* Photoresponse of CsPbBr3 and Cs4PbBr6 Perovskite Single Crystals. *J Phys Chem Lett* **8**, 565-570, (2017).
7. Liu, J. J. *et al.* All-Inorganic Perovskite Quantum Dots/p-Si Heterojunction Light-Emitting Diodes under DC and AC Driving Modes. *Advanced Optical Materials* **6**, 1700897, (2018).
8. Maddalena, F., Chin, X. Y., Cortecchia, D., Bruno, A. & Soci, C. Brightness Enhancement in Pulsed-Operated Perovskite Light-Emitting Transistors. *ACS Appl Mater Interfaces* **10**, 37316-37325, (2018).
9. Yarita, N. *et al.* Dynamics of Charged Excitons and Biexcitons in CsPbBr3 Perovskite Nanocrystals Revealed by Femtosecond Transient-Absorption and Single-Dot Luminescence Spectroscopy. *J Phys Chem Lett* **8**, 1413-1418, (2017).